

A study of strains in abraded diamond surfaces

BY F. C. FRANK, F.R.S., B. R. LAWN,[†] A. R. LANG
H. H. Wills Physics Laboratory, University of Bristol

AND E. M. WILKS
Clarendon Laboratory, University of Oxford

(Received 10 March 1967)

[Plates 25–27]

The nature of surface damage suffered by diamond during abrasion processes has been studied by X-ray topographic analysis of the strain patterns in and around microabrasion patches on cube, dodecahedron and octahedron surfaces of highly perfect natural diamonds. The strain field has been computed from an elastic model assuming that the abrasion leaves a thin surface layer of crystal in a state of residual compression. The observed diffraction contrast agrees well with this model. From the contrast patterns the stresses in the surface, expressed as force in the surface acting normally to unit length in the surface, lie in the range 1×10^5 to 5×10^5 dyn/cm, with little dependence upon orientation of the abrasion. The evidence strongly favours a microcracking mechanism for abrasive wear of diamond.

1. INTRODUCTION

The pronounced anisotropy of hardness in diamond has been of interest to diamond polishers for a great number of years. The degree of anisotropy measured is largely dependent on the experimental conditions, and it has become clear that different tests measure different properties of the material. For instance, Seal (1958) performed a 'scratch' test by sliding a diamond stylus across a specimen surface and observing the minimum load required to produce a fracture track. Direction of sliding on any one face was found to have only a small influence on this critical load, as one may indeed expect on theoretical grounds (Lawn 1967). On the other hand, hardness measurements based on the rate of removal of material in abrasion tests show anisotropies of rate by factors of up to 500. Clearly the scratch test measures the ease of crack production, whereas the abrasion method records the ability of a grinding particle to dislodge fragments of specimen: even though both mechanisms may be basically fracture processes it does not follow that they should exhibit the same anisotropy.

Apart from the practical importance to the diamond polishers the understanding of abrasion behaviour is fundamental to the understanding of mechanical properties of brittle surfaces in general. Diamond is known to cleave in a highly brittle manner on {111} planes, and fracture must also occur on secondary cleavage planes, or even on non-crystallographic surfaces, in Hertzian-type stressfields (Howes & Tolansky 1955; Frank & Lawn 1967). The possibility of plastic deformation of diamond at temperatures below 1500 °C appears remote according to the experiments of Evans & Wild (1965, 1966). Unless, therefore, high temperatures are

[†] Now at Division of Engineering, Brown University, Providence, Rhode Island 02912, U.S.A.

achieved as the diamond stylus or abrading particle traverses the specimen surface the possibility of plastic flow as a means of surface deformation must be considered highly unlikely, as must other temperature-dependent mechanisms such as surface graphitization of the diamond. The observation by Wilks & Wilks (1959) that the abrasion rate of diamond is independent of the speed of the abrading wheel appears to rule out any thermal process, leaving fracture as the most probable means of explaining surface deformation processes. This conclusion is in conformity with Tolkowsky's (1920) proposal that small fracture fragments, octahedral or tetrahedral in shape and bounded by the 'easy cleavage planes', are removed by the abrading particles. Wilks & Wilks have used Tolkowsky's hypothesis, in a modified and more realistic form, to explain all features of abrasion anisotropy on diamond surfaces, the fragments being more easily removed in certain directions than in others. On the other hand, it is possible that attrition of diamond surfaces may occur on an atomic scale under certain conditions: such is indicated by the experiments of Seal (1965) in which a lightly loaded stylus was rubbed up to 10^6 times along a given path. However, these latter experiments were performed at loads much smaller than those required to produce cracking of the surface, and it appears clear that attrition will be dominated by fracture processes at high loads.

A fracture mechanism has also been proposed (Preston 1922) to explain the surface deformation and abrading properties of glass. (Analogies between glass and diamond must be treated with caution however, since evidence suggestive of plastic flow (see, for example, Marsh 1964) and thermal effects has been found in glass when very fine polishes are used.) The mode of deformation, as for diamond, when a particle slides across the glass surface, is one of surface cracking in which the depth of damage is of the order of the size of the particle, and abrasion is explained by fragmentation after several such particles have created an intersecting network of cracks. (Such a mechanism has, of course, its analogue in diamond abrasion in the form of the Tolkowsky proposal.) One of the features of abraded glass surfaces (the so-called 'greyed' surfaces) which has received considerable attention is the surface strain introduced as a result of the surface fractures: 'debris' at the fracture interfaces prevents perfect healing of the cracks and a state of residual elastic compression exists in the glass surface. This effect, first noted by Twyman (1905), through the appearance of birefringence, and known thereafter as the Twyman effect, was measured mechanically by Dalladay (1922), as a force acting along a line in the surface, by observing the degree of bending of a glass strip abraded on one face. Surface line forces of the order 10^5 to 10^6 dyn/cm were obtained for a range of abrasive size from 15 to $400\text{ }\mu\text{m}$.

Natural diamonds exhibit strong evidence of residual strain at surface fractures such as ring cracks both natural (Lang 1964) and laboratory-produced (Lawn & Komatsu 1966), so one would expect abraded diamond surfaces to exhibit a Twyman effect if surface cracking were the predominant surface deformation process during abrasion. The almost ubiquitous presence of strain birefringence distributed within the volume of diamond specimens (Tolansky 1966; Lang 1967) makes direct optical observation of surface birefringence effects difficult. However, one can abrade small regions, elliptical in shape, on diamond surfaces using a

microabrasion technique; the strain field in the surrounding crystal produced by such regions is ideally suited to an investigation by the extremely sensitive X-ray topographic methods. Such an investigation is described in the following sections. Although one cannot infer directly the mechanism of abrasion by a study of this kind, the nature and extent of surface damage under normal diamond abrasion conditions can be shown to be consistent with a fracture mechanism.

2. ELASTIC STRAIN FIELD ABOUT A MICROABRASION

The microabrasion test has been described in detail elsewhere (for instance, Wilks & Wilks 1965) and only the immediately relevant features will receive attention here. A small cast-iron grinding wheel, in the shape of a truncated bi-cone with included angle 110° at the grinding edge, is charged with a mixture of diamond powder in olive oil and set rotating about its axis, at several thousand revolutions per minute, just above the diamond surface. The wheel is then made to bear, under load, upon the specimen for a period of several seconds. The iron wheel becomes effectively flattened against the relatively hard diamond surface over an approximately elliptical area of contact whose semi-axes, a and b , say, typically measure some hundreds of microns. The depth of the resulting abrasion cut is usually of order $1\text{ }\mu\text{m}$ so that one may consider, to a reasonable approximation, the abraded patch as a flat elliptical disc of 'bad' material embedded into the surface of an otherwise undeformed elastic medium. The table gives average dimensions and test details of several cuts (to be discussed in detail later) made in both 'easy' and 'hard' grinding directions on several different surface orientations on three stones of gem quality.

TABLE 1

average dimension of abrasions

crystal face	abrading direction	average dimension of abrasions			F' (dyn/cm)
		length (mm)	breadth (mm)	depth	
(001) polished	[100] easy	0.37	0.18	$1.7\text{ }\mu\text{m}$	2×10^5
(001) polished	[110] hard	0.35	0.21	$< 100\text{ }\text{\AA}$	3×10^5
(111) natural	[112] hard	0.27	0.17	$0.1\text{ }\mu\text{m}$	5×10^5
(110) polished	[001] easy	0.60	0.27	$4.5\text{ }\mu\text{m}$	1×10^5

$\frac{1}{2}$ in. radius cast iron biconical grinding wheel, included angle 110° , rotating speed 5000 rev/min, abrasive size 0 to $1\text{ }\mu\text{m}$, duration of abrasion 20 s.

Let us now consider the strain field surrounding a microabrasion on the basis that the bad material is in a state of compression. We take the elliptical disc to have thickness δ ; if surface cracking followed by imperfect crack closure be the source of surface compression, δ is of the order of the penetration depth of microcracks, or of the diameter of abrading particles, and is small compared with a and b . In general, one must suppose that this compressive stress will vary with direction—if the cracks were all parallel the stress would be essentially uniaxial. However, the microcracks observed along single scratches have, crudely speaking, semi-circular traces (Lawn 1967) and may therefore be expected to produce compressive

stress in all directions parallel to the free surface: moreover, their presence will make the material weak in shear about any axis normal to the free surface, tending to equalize the horizontal pressures. We therefore proceed with the simplified assumption of two-dimensionally isotropic compressive stress in the damaged layer. Let us consider first a layer of such damaged material to extend across the entire surface of a semi-infinite elastic medium. There can then be no stress acting across the interface between damaged and undamaged material. In reality, of course, as for uniformly abraded surfaces of real specimens, the stresses may be relaxed at the edges of the finite surfaces; with thin specimens this may be manifested as a 'bowing' of the entire specimen, as in Twyman's & Dalladay's experiments (see § 1). With localized patches (figure 1) of bad material the residual stress may be partially relieved by distortion of the surrounding matrix material when the thickness of the

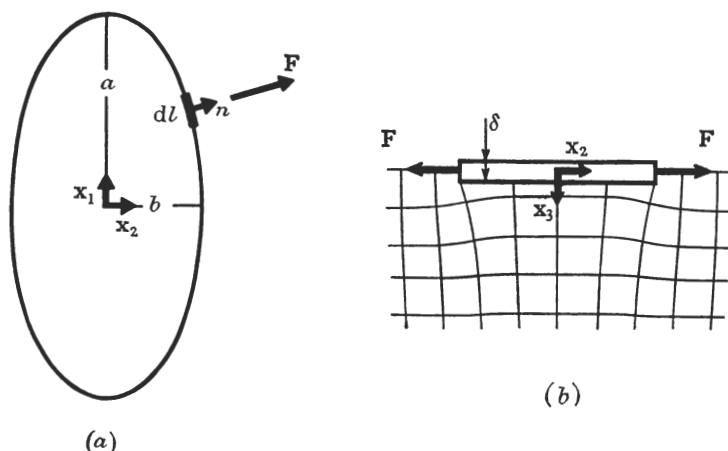


FIGURE 1. Surface view (a) and cross-sectional view (b) of elliptical abrasion patch on diamond. Explained in text.

specimen greatly exceeds the dimensions of the patches. The elliptical disc of damaged material exerts an outward normal pressure p on the matrix, acting across its peripheral bounding surface which is an elliptic cylindrical strip of width δ . Since δ is small compared with the other dimensions of the disc we may, except at distances comparable with δ from the periphery of the abrasion patch, consider this pressure to be replaceable by a line force \mathbf{F} per unit length of periphery, acting in the direction of \mathbf{n} , a unit vector lying in the surface and directed perpendicularly outward from the periphery, as shown in figure 1: \mathbf{F} may therefore be written as $\mathbf{F} = F\mathbf{n} = p\delta\mathbf{n}$.

The strain field is calculated from the expressions of isotropic elasticity theory for the displacements at any point in a semi-infinite medium due to a force applied at a point in the surface. Using Cartesian coordinates defined by unit vectors $\mathbf{x}_1, \mathbf{x}_2, \mathbf{x}_3$ as shown in figure 1, and following Landau & Lifshitz (1959), we can write the component u_i of the displacement vector \mathbf{u} at (x_1, x_2, x_3) due to a point force at the origin as

$$u_i = G_{ik}(x_1, x_2, x_3) F_k, \quad (2.1)$$

where the G_{ik} involve the Young modulus and the Poisson ratio and are given

by equations 8.18 of Landau & Lifshitz; k is a repeated suffix. Writing $\mathbf{F}d\mathbf{l}$ as an effective point force we may then integrate round the periphery of the abrasion patch to find the total displacements at (x_1, x_2, x_3) :

$$u_i = F \oint G_{ik}(x_1 - x'_1, x_2 - x'_2, x_3) n_k d\mathbf{l}, \quad (2.2)$$

in which n_k is the component of \mathbf{n} in the direction \mathbf{x}_k and the coordinates of $d\mathbf{l}$ are $(x'_1, x'_2, 0)$. The assumption that F is independent of location of $d\mathbf{l}$ on the periphery is for present purposes a reasonable approximation; its justification will be discussed further below. The numerically calculated displacement field in the plane $x_1 = 0$ is shown schematically, for an arbitrarily large value of F , in figure 1(b), in the form of a distorted lattice. These calculations apply to an ellipse having an axial ratio corresponding to the first cut listed in table 1. The displacements are insensitive to variations of the ratio within the range covered by the cuts listed in the table. The strain terms $\partial u_i / \partial x_j$ are readily found from equation (2.2) by numerical methods.

We may now look more closely at the situation under the rotating micro-abrading wheel and attempt to relate this to the elastic model we have adopted above. If the wheel were to be free of diamond powder and were to suffer no inelastic deformation the diamond specimen would be subjected to a stress distribution similar to that whose maximum tensile values are shown by the contours in figures 11 to 13 in Hamilton & Goodman (1966); that is, a stress field much more strongly tensile near that end of the major axis of the cut where the grinding edge of the wheel enters (leading edge) than near the end where it leaves (trailing edge). Since the wheel is lubricated with olive oil the coefficient of friction is probably about 0.1. This is lower than the values considered by Hamilton & Goodman but it still leads to a considerable enhancement of tensile stress near the leading edge, as can be seen by reference to the stress contours in a semi-infinite elastic medium upon whose surface a spherical indenter slides with coefficient of friction equal to 0.1 (Lawn 1967, figure 1a). However, tensile stresses much greater than the above will be developed under individual small particles wedged into the abrading wheel, for it may be shown from the Hertz elastic theory of contact that the stresses under a particle of (mean) radius r are proportional to $r^{-3/2}$ for a given load. The principal damage will therefore be caused by the abrading particles themselves, and the load on each particle will vary from a maximum at the centre of contact in figure 1 to zero at the edge. Despite this dominance of the individual-particle stress fields, the superposed frictional stresses due to the wheel rotation will be expected to suppress somewhat the damage process at the trailing edge of the cut, and likewise to enhance it at the leading edge, if cracking due to tensile stresses is the dominant mechanism. The plane $x_2 = 0$ is nevertheless a plane of symmetry of the strain field and the displacements depicted in figure 1(b) may be regarded as relatively unaffected by an asymmetry in damage as discussed above. For this reason the measurements of strain discussed in the next section will be confined to the $x_1 = 0$ plane, with the knowledge that this strain represents, for a given cut, an approximate mean of the strain distribution in any plane containing \mathbf{x}_3 .

3. X-RAY TOPOGRAPHY OF MICROABRASIONS

The lattice distortions in and around microabrasions can be studied by both reflexion and transmission X-ray topographs. In the reflexion case, and with low or moderate absorption in the transmission case, lattice distortion produces positive diffraction contrast, i.e. enhanced diffracted intensity, under the usual experimental conditions in which the angular divergence of the incident X-ray beam is large compared with both the very narrow angular reflecting range of the perfect crystal (typically a few seconds of arc) and the range of misorientations in the crystal specimen. On the topographs shown here (which, as is customary, are reproductions of the original plates) the positive diffraction contrast appears as extra blackening. Topographs giving a picture of the abrasion patch can be recorded with little geometric distortion by using the reflexion arrangement when suitably oriented Bragg planes and high Bragg angles are chosen. The latter can be obtained with strong, low-order Bragg reflexions by use of soft radiations such as $\text{CuK}\alpha$ and $\text{CrK}\alpha$ (Newkirk 1958). Transmission topographs taken by the projection topograph technique (Lang 1959) give almost undistorted pictures of the abrasion patches when Bragg planes nearly normal to the crystal face are used together with small Bragg angles such as occur when the harder radiations $\text{MoK}\alpha$ and $\text{AgK}\alpha$ are employed. These harder radiations are also generally necessary for penetration of the transmission specimen, but, in the case of diamond, specimens up to 2 or 3 mm thick can be used with $\text{CuK}\alpha$ radiation without excessive absorption losses. The soft radiations used in reflexion topographs of perfect (or nearly perfect) diamond do not effectively penetrate the specimen to a depth of more than one or two extinction distances (a depth of typically a few microns). Compared with the harder radiations they produce less extensive diffraction contrast from a given distorted region, and shorter-range photoelectron tracks in the nuclear emulsions with which the topographs are recorded. Hence the best topographic resolution is obtained in soft-radiation reflexion topographs: detail down to about $1\mu\text{m}$ can be resolved. The transmission topographs are less sensitive to surface distortions on the micron scale, and are quite insensitive to incidental features such as specimen surface contour. The interpretation of the diffraction contrast of transmission topographs in terms of the crystal strain fields is somewhat simpler than in the reflexion case, but it can never be as simple as in transmission electron microscopy. This is because in X-ray projection topographs the diffracted X-ray intensity leaving each point on the X-ray exit surface of the specimen receives contributions from rays whose directions in the specimen lie within the whole 'energy-flow triangle' contained between the relatively widely separated direct and diffracted beam directions, instead of just from a single 'column' as in the electron case (see, for example, Takagi 1962). Complications in image structure arising from the width of this triangle become less serious as the diffraction angle is reduced. Most of the quantitative work in the present study was done with 220 reflexions of $\text{MoK}\alpha$ radiation for which the Bragg angle is moderately low ($\theta = 16^\circ$). A transmission topograph image will be a projection not only of the abrasion patch, which lies on the X-ray exit surface of the specimen, but also of any lattice imperfections

lying between this surface and the X-ray entrance surface of the specimen. In order to remove unwanted contributions to the image, the transmission topographs shown here were taken using the technique of 'limited projection topographs' (Lang 1963) in which diffracted beams originating from regions not of interest were prevented from reaching the photographic plate. It should be emphasized, however, that the experiments were performed on stones carefully selected for their unusually high lattice perfection: they showed very little birefringence, their natural octahedron surfaces were almost free of pyramidal trigons, and subsequent X-ray topographic surveys confirmed them to be substantially free of dislocations and other defects which produce long-range strains. In all topographs reproduced the arrows indicate the projection of the reciprocal lattice vector \mathbf{g} on to the image plane. The dimensions of the microabrasions shown here are listed in table 1.

3.1. *Reflexion topographs*

Figure 2, plate 25, shows a reflexion topograph of a polished cube face of diamond containing three microabrasions, two made in an easy grinding direction and one in a hard grinding direction. The as-polished face reveals no diffraction contrast, indicating a fine degree of polishing. (Note, however, that small patches of damage due to 'false starts' of the microabrading wheel appear in the field, the most noticeable being in the upper right-hand part of the figure. These patches show the same contrast effects as appear inside the intentional microabrasions themselves.) More crudely polished surfaces often show the type of contrast seen within the microabrasions here: indeed, on such surfaces the individual microcracks within each striation may be occasionally resolved (Lawn & Komatsu 1966). In figure 2 striations may be resolved within the two similar abrasion cuts, where the striations lie parallel to the plane containing the incident and diffracted beams, but not in the third cut. This is purely a result of the diffraction geometry, arising from the spreading of rays within the wide energy-flow triangle ($2\theta = 130^\circ$). In other Bragg reflexions striations within the third cut can be as well resolved as in the soft-direction pair in figure 2. Optical phase-contrast microscopy reveals a one-to-one correspondence between the striations on the topographs and the polish tracks on the specimens. The dark bands of enhanced contrast near the periphery of the microabrasions are ascribed to the large, long-range lattice distortions there (cf. figure 1*b*), and will receive more attention in the following sections.

One important feature emerges from figure 2. The easy and hard directions on the cube face represent extremes of grinding ease, as may be seen by comparing the depths of cuts listed in the table. Yet all abrasion patches show comparable diffraction contrast within the abraded area, indicating that the degree of surface damage is reasonably independent of direction of abrasion, in complete contrast to the wear rate. The single cut in the hard direction was in fact so shallow as to be barely detectable with the most sensitive optical techniques. This emphasizes the ability of X-ray diffraction methods to detect small amounts of damage on crystal surfaces.

3.2. *Transmission topographs*

The same microabrasions on the polished cube face are shown in the transmission topographs of figure 3, plate 26. These were taken with $\text{MoK}\alpha$ radiation, Bragg planes being normal to the cube face. The low absorption condition $\mu t < 1$ (μ = linear absorption coefficient, t = specimen thickness) is satisfied, permitting strong 'extinction' contrast to develop in distorted regions. Such strong contrast is indeed observed coming from the regions of large, long-range strain gradients near the peripheries of the cuts. This is a topographic illustration of the enhancement of diffracted intensity known as the 'Fukushima effect' which was recorded at the boundary between ground (i.e. surface-damaged) and etched (i.e. damage-free) areas on quartz plates (Fukushima 1954). The contrast falls to zero when the condition $\mathbf{g} \cdot \mathbf{u} = 0$ is satisfied, where \mathbf{u} is the displacement vector and \mathbf{g} is the reciprocal lattice vector. The major features of figure 3 may now be related to the elastic model proposed in §2:

(a) The contrast is zero at positions on the elliptical periphery where $\mathbf{g} \cdot \mathbf{n}$ is zero, and is greatest roughly where $\mathbf{g} \cdot \mathbf{n}$ is a maximum. This is in accord with the model, which would predict that \mathbf{u} is very nearly confined to the plane defined by \mathbf{n} and \mathbf{x}_3 .

(b) The contrast is asymmetrical about the minor axis of the abrasions. The leading edges of the cuts show an enhancement of strain, as predicted in §2. Note that the asymmetry is less for the cut made in the hard direction. Seal (1958) has found that the friction on diamond varies in different directions on a given cube face (usually by a factor of about 2), attaining a maximum in the easy grinding direction and a minimum in the hard one: as pointed out in §2 the asymmetry effect would be expected to decrease with decreasing friction.

(c) By comparison with optical micrographs it is found that the peripheral contrast extends about equally on either side of the actual elliptical boundaries of the cut. (In the weaker, 400-type reflexions the width of the band of peripheral contrast is greater than in the stronger, 220-type reflexions. This is explained in §4.)

Thus the topographs provide evidence in support of the model of §2. It remains to establish the sense of \mathbf{F} , or \mathbf{u} . The contrast effects in topographs taken with negligible X-ray absorption are insensitive to a reversal of \mathbf{g} . But this is not so when μt is in the range 3 to 5, as in the pair of transmission topographs of figure 4, plate 25, taken with $\text{CuK}\alpha$ radiation. They show part of another cube face containing easy-direction cuts which are almost identical with those of figure 3. Both positive and negative diffraction contrast appear in the images and, making some allowance for the asymmetry of the strain distribution about the minor axis of the ellipse, it can be said that the contrast distribution in figure 4(a) is an inversion of that in figure 4(b). In these and other topographs taken under similar conditions net positive contrast occurs in the regions near the periphery where $\mathbf{g} \cdot \mathbf{n}$ is positive. The explanation of this pattern is discussed in §4, but its interpretation to give the sense of \mathbf{F} may be made purely empirically by reference to X-ray topographs, taken under conditions of moderate absorption, of strips of oxide and evaporated metal films on silicon surfaces (Meiran & Blech 1965). The oxide and metal films are

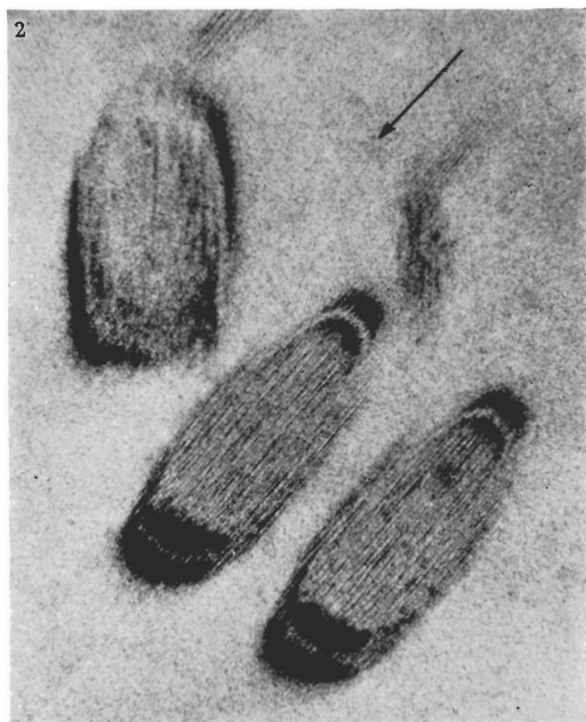


FIGURE 2. Reflexion topograph of polished (001) face of diamond. $\text{CrK}\alpha$ radiation, 202 reflexion. The Bragg plane makes 45° with the specimen surface. Two cuts parallel to $[100]$, one cut parallel to $[110]$.

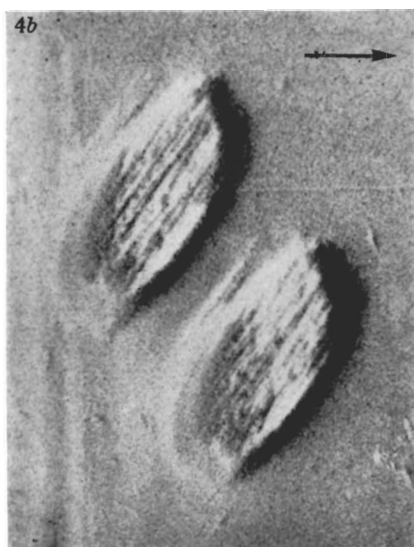
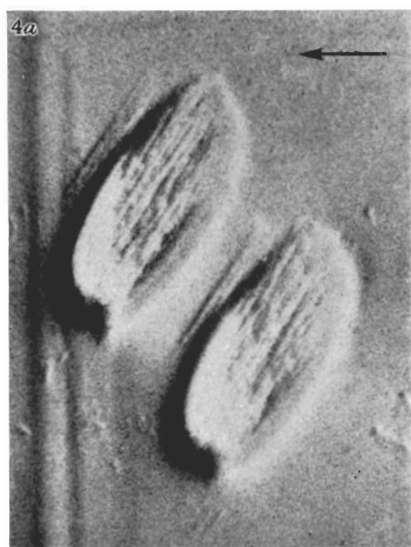


FIGURE 4. Transmission topographs of a second polished (001) face. Cuts parallel to $[100]$. $\text{CuK}\alpha$ radiation, (a) $\bar{2}20$, (b) $2\bar{2}0$: stereopair of reflexions.

(Facing p. 216)

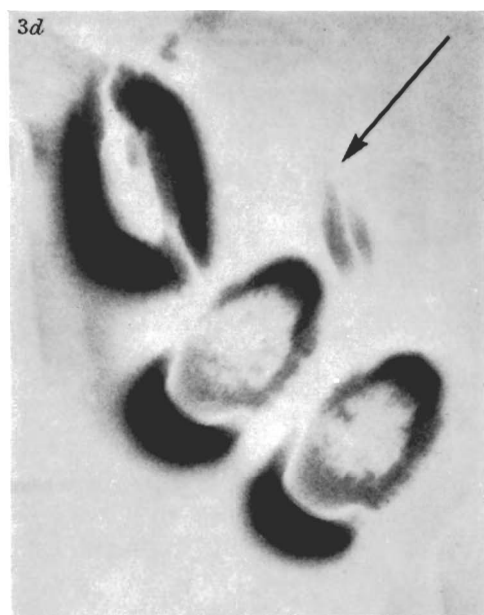
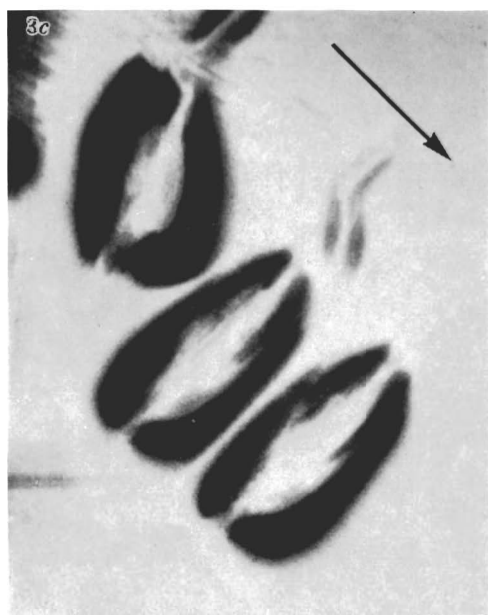


FIGURE 3. Transmission topographs of same face shown in figure 2. MoK α radiation, (a) 220, (b) 220, (c) 040, (d) 400 reflexions.

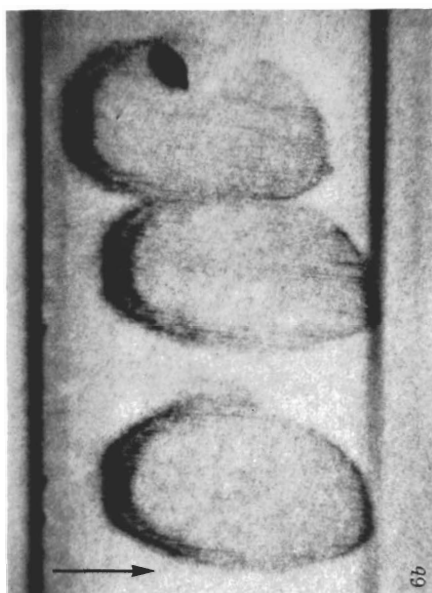
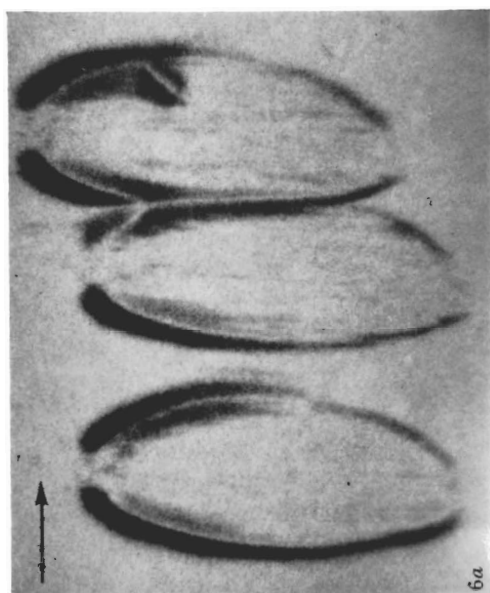


FIGURE 6. Transmission topographs of polished (110) face of diamond. Cuts parallel [001]. MoK α radiation, (a) 220, (b) 111 reflexions.

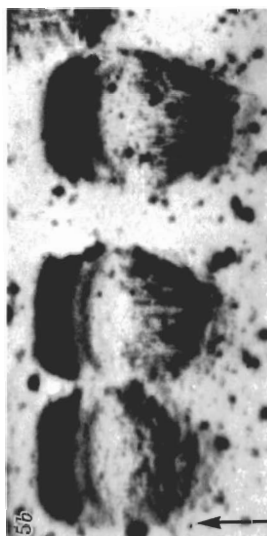
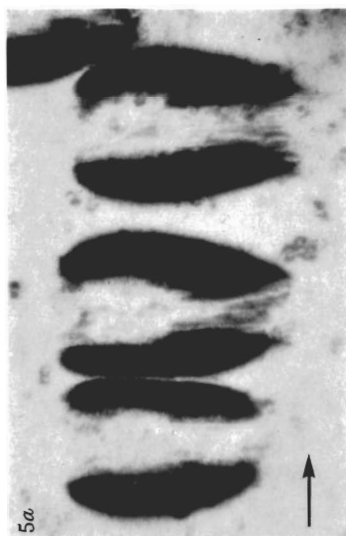


FIGURE 5. Transmission topographs of natural (111) face of diamond. Cuts parallel to [112]. MoK α radiation, (a) 220, (b) 220 reflexions.

known to produce surface forces directed in positive and negative directions of \mathbf{n} , respectively. The edges of these strips exhibit a marked Fukushima effect, and show the stronger net positive contrast where $\mathbf{F} \cdot \mathbf{n}$ and $\mathbf{g} \cdot \mathbf{n}$ have the same sign. Figure 4 accordingly indicates that $\mathbf{F} \cdot \mathbf{n}$ is positive, confirming the assumption that the abrasion process leaves the diamond surface in a state of residual compression.

The description given above of observations on cube faces applies equally well to cuts on octahedral and dodecahedral surfaces, as listed in the table. On the topographs of the natural octahedral face (figure 5, plate 27) specks of diffraction contrast due to natural percussion damage are evident. The lines of blackening running across figure 6(b), plate 27, perpendicular to \mathbf{g} arise from stress relief where growth layers parallel to octahedral planes outcrop on the polished dodecahedral face. Such outcrops have been previously described (Lawn, Kamiya & Lang 1965).

4. EVALUATION OF THE STRAIN FIELD

Several distinguishable contrast-producing mechanisms contribute to the abrasion image structures, and it is in terms of their varying relative contributions that the diversity of images may be understood. In certain situations this understanding can be quantitatively developed to lead to an evaluation of the strain field. It should be remembered that in the X-ray topographic experiments the incident wave has a divergence well in excess of the angular range of glancing angles producing observable intensity of a given Bragg reflexion. Hence at its entrance into the crystal this spherical incident wave excites Bloch waves whose wave vectors cover an appreciable region of the dispersion surface, on either side of the Brillouin zone boundary. The Bloch waves form a fan of rays which, propagating along the normal to the dispersion surface at the 'wave-points' defined by their particular wave vectors, fill the whole energy-flow triangle mentioned in §3. In an undistorted crystal the ray paths are straight lines, but in a distorted crystal the rays bend because the wave-points migrate along the dispersion surface as their wave vectors change in orientation with respect to the 'local' reciprocal lattice. If the Bragg planes are curved the rays belonging to branch (1) of the dispersion surface (the branch with longer wave vectors) have a curvature in the same sense as the Bragg planes, whereas branch (2) waves (shorter wave vectors) are oppositely curved (Penning & Polder 1961; Kato 1963*a, b*, 1964*a, b*). This 'energy-flow refraction' noticeably affects the topograph image as soon as the intensity associated with branch (1) of the dispersion surface begins to dominate over that of branch (2) through anomalous absorption, as it does in even-index reflexions of the diamond structure with $\mu t > 1$ (μ is the *normal* linear photoelectric absorption coefficient). The diffraction contrast then produced at a particular point on the image arises from both the spatial redistribution of rays reaching the specimen exit surface, resulting from their curved paths within the energy-flow triangle, and the change in partition of ray energy between direct and diffracted beam directions resulting from the *difference* in deviation from exact satisfaction of the Bragg condition by the Bloch wave constituting the ray,

measured at its respective incident and exit points on the specimen surfaces. Both positive and negative contrast may be produced, with a dependence upon the sign of \mathbf{g} . Such effects are illustrated by figure 4. If the crystal distortion is severe then the energy of a given Bloch wave may be scattered into other waves belonging to either branch of the dispersion surface. Under conditions of low X-ray absorption the distribution of energy among Bloch waves excited by the incident beam is such that interbranch scattering will cause a strong increase in intensity of the diffracted beam leaving the crystal. Calculations such as those of Penning (1966) show that the interbranch scattering becomes substantial when the curvature of the Bragg planes in the plane of incidence rotates \mathbf{g} by more than $\Delta\theta_{\frac{1}{2}}$ (half the angular range of reflexion, measured at half maximum intensity) in a path length of one extinction distance, ξ_g , along the ray trajectory. (Since $\Delta\theta_{\frac{1}{2}} = (g\xi_g)^{-1}$ this critical radius of curvature, R_c , is expressible as $R_c = g\xi_g^2$. With X-rays, ξ_g is proportional to $F(hkl)\lambda/\cos\theta$, $F(hkl)$ being the structure factor of the reflexion hkl .) However, for strain fields in which the lattice misorientation increases very rapidly as the strain centre is approached (dislocations, and the peripheries of abrasions here discussed are examples of this class) a simpler criterion for the commencement of significant interbranch scattering may be applied, and it accounts well for dislocation image widths in the low absorption case. It is simply that the local tilt of the lattice should have a component that rotates \mathbf{g} in the plane of incidence through an angle about equal to $\Delta\theta_{\frac{1}{2}}$, measured with respect to the 'perfect' matrix far away from the strain centre. Closer to the strain centre, where this tilt is exceeded, the distortion increases so rapidly that kinematic diffraction conditions apply: the crystal there becomes effectively 'mosaic'.

The transmission topographs taken with $\text{MoK}\alpha$ radiation, which well satisfy the condition $\mu t < 1$, have been interpreted with the tilt criterion, but attention has also been paid to the contribution of lattice dilation to the deviation from the Bragg condition. (Dilation was ignored, and Bragg plane curvature considered only, just to simplify description in the discussion above.) Let us consider a wave coming upwards from the undistorted crystal below the abrasion whose cross-section is shown in figure 1(b), and suppose that Bragg reflexion is occurring at planes normal to \mathbf{x}_2 . Measured with respect to crystal remote from the abrasion we may define a local 'effective tilt', ϕ , given by

$$\phi = \mp \frac{\partial u_2}{\partial x_3} + \tan \theta \frac{\partial u_2}{\partial x_2}, \quad (4.1)$$

where the minus sign applies when \mathbf{g} is parallel to \mathbf{x}_2 , and vice versa. Positive ϕ indicates a change in satisfaction of the Bragg condition in the same sense as an increase in glancing angle of incidence upon the Bragg planes. The first term on the right-hand side of equation (4.1) represents the component of lattice rotation about \mathbf{x}_1 as axis: its contribution to ϕ reverses in sign with change in sign of \mathbf{g} . The second term, the dilation term, is relatively small for low Bragg angles. The dominance of the tilt term is well demonstrated in figures 5(a) and 6(a). In regions where the strain fields of the rather closely adjacent abrasions overlap there is a separating line of no contrast. Now if tilting were the dominant contrast-producing

factor, one would indeed expect no contrast in this region, because of the mutual cancellation of tilts. Dilation effects, on the other hand, would receive mutual reinforcement.

Figure 7 is a plot, in the plane $x_1 = 0$, of contours of the parameter $(E/F)\phi$, ϕ being given by equation (4.1), for the value of $\tan\theta$ appropriate for the 220 reflexion of MoK α radiation. To use plots such as this, we find the value of $(E/F)\phi$ that best fits the observed width of the band of blackening on the topograph image of the abrasion periphery, and we set ϕ equal to the calculated value of $\Delta\theta_{\frac{1}{2}}$ for the

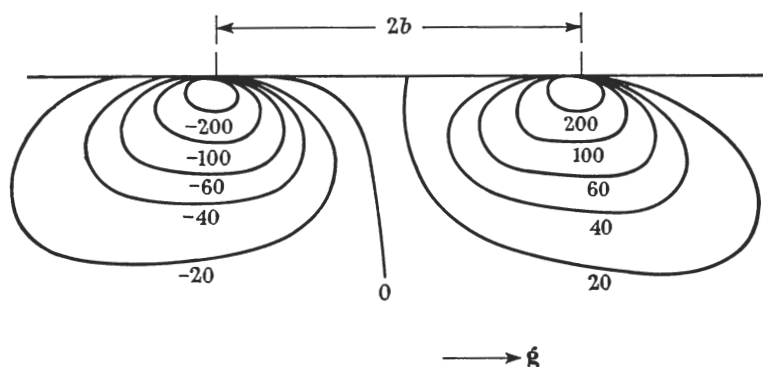


FIGURE 7. Plot of deviation parameter $(E/F)\phi$ in units of radians/cm, on the plane $x_1 = 0$, calculated for the dimensions representative of the abrasions on the cube faces, using the 220-type reflexion with MoK α radiation.

reflexion concerned. Taking E to be 10^{13} dyn/cm 2 , F is then determined. Contour plots such as figure 7 were constructed for each of the cuts listed in the table, using the appropriate values of a , b and $\tan\theta$. Average values of F so found are given in the final column of the table. As long as the dilation term in equation (4.1) is small its contribution is apparent merely as a small departure from anti-symmetry of the contours about the plane $x_2 = 0$: the maxima of $|\phi|$ are displaced slightly towards the direction $-\mathbf{g}$; and thus with contrast occurring when $|\phi|$ exceeds $\Delta\theta_{\frac{1}{2}}$, changing the sign of \mathbf{g} has but little effect on the width and position of the bands of blackening, which extend nearly equally on both sides of the elliptical periphery. This is in agreement with observations made when adsorption is negligible, as described in §3.

The dependence of $\Delta\theta_{\frac{1}{2}}$ upon wavelength indicates that when a change is made from MoK α (0.71 Å) to CuK α (1.54 Å) in observing, say, the 220 reflexion, the magnitude of the critical contour $(E/F)\phi$ will be about doubled. Figure 7 then predicts a rough halving of the width of the image of the periphery and a reduction by a factor of about four in the volume of the 'kinematic' region in which misorientation exceeds $\Delta\theta_{\frac{1}{2}}$. This reduction, together with the relative suppression, by absorption, of rays not closely satisfying the Bragg condition when $\mu t \sim 3$ to 5, greatly lessens the contribution of this region to the images shown in figure 4. In these, as already mentioned, 'energy flow refraction' is important, and causes both redistribution of intensity across the image and net changes in contrast depended upon the sign of \mathbf{g} . Now the strain field depicted in figure 1(b) does not

provide a rotation of the lattice planes at the free surface because there is no surface slope, and, of course, there can be no shear about axes in the surface. With no significant *difference* in deviation from the Bragg condition between that at entrance and exit surfaces it is at first sight difficult to explain the *net* positive contrast in the sector of the periphery where $\mathbf{g} \cdot \mathbf{n}$ is positive. The explanation lies in the spacing of the contours in figure 7. They become very close to each other just under the surface on either side of the periphery, showing that the tilt existing below the surface returns to its surface-value, zero, quite sharply. Now the extinction distance for the 220 reflexion of $\text{CuK}\alpha$ radiation is $24\mu\text{m}$, i.e. one-eighth of the distance $2b$ in figure 7. When the change in Bragg-plane tilt occurring between the exit surface and a level $24\mu\text{m}$ below it exceeds $\Delta\theta_{\frac{1}{2}}$, the critical curvature, R_c^{-1} , is exceeded. Thus the dominant branch (1) waves, which, in the sector where $\mathbf{g} \cdot \mathbf{n}$ is positive, have been bent towards the diffracted beam direction while passing through the long-range strain field extending deep below the periphery, cannot have that bend completely reversed by the layers just below the surface; they partly 'tunnel' through these layers and contribute extra energy to the diffracted beam.

Certain fine structure is evident in some images of the periphery. The enhancement of diffraction contrast around the leading edge of the cut is sometimes accompanied by a splitting of the peripheral band of blackening. This is seen in the transmission topographs in figures 5(a), 6(a) and 6(b). Now, as mentioned in §2, frictional stresses under the rotating wheel should enhance cracking at the leading edge of the cut and somewhat suppress it at the trailing edge. A thin crescent of extra heavy cracking, and hence of extra compressive stress, is believed to be present at the leading edge of the abrasion patch. The lattice tilts generated by this extra stress, when added to those due to the elliptical disk already considered, would produce a reduction of tilt (possibly even a reversal in some sectors) at the concave edge of the crescent. The local minimum in tilt magnitude would account for the dip in diffracted intensity which divides the band of blackening. On the other hand, it is likely that the double maxima of blackening at both leading and trailing edges of the cut seen in the reflexion topograph figure 2 (most distinctly in the cuts whose long axis is parallel with the projection of \mathbf{g}) arise mainly from the much greater importance of the dilation term of equation (4.1) in this case. The factor $\tan\theta$ is larger than in the transmission topographs just considered by a factor of 10 for the 220 reflexions and 16 for the 111 reflexions. The dilation term changes sign under the periphery (as can be seen from the schematic representation of the lattice displacements in figure 1(b)), and this will produce a local minimum of $|\phi|$, and hence of blackening, when dilation is dominant.

5. CONCLUSION

The values obtained for F lie in the range 1×10^5 to 5×10^5 dyn/cm. Since $F = p\delta$, and δ may be taken to be in the range 10^{-4} to 10^{-3} cm typically, we obtain $p \sim 10^9$ dyn/cm², which represents a surface strain of order 0.1% near the abrasion periphery. With F roughly known we can calculate the corresponding

magnitudes of the displacements sketched in figure 1(b) and determine whether they should be optically observable. The elastic model predicts that the material within the elliptical boundary be raised with respect to the surrounding matrix, but in all cases considered here the elevation is less than 10 Å and, being small compared with the depth of material removed during abrasion, would be unobservable. More important is the predicted flatness of the area surrounding the abrasion: there is a complete absence of 'pile-up' such as is, for instance, often observed around indentations and abrasions on soft materials which deform plastically. This flatness accords, within the limits of the most sensitive optical interferometric techniques, with measurements on many abrasions on diamond (Tolansky & Austin 1949; Wilks & Wilks 1965); and in the present specimens we have similarly been unable to detect any pile-up by optical methods.

It has been pointed out by Roesler (1956) that when Auerbach's law (that the critical normal load for fracture is proportional to the radius r of indenter) is obeyed the critical fracturing stresses below a spherical indenting particle must vary as $r^{-\frac{1}{2}}$ and may ultimately, for small enough r , exceed the cohesive strength of the material. Seal (1958) suggests that for particles of micron size this may lead to an abrasion mechanism in which interatomic bonds are disrupted individually rather than by a crack-propagating mechanism. However, more detailed calculations of the critical normal loads required to produce surface fracture when a spherical particle is made to slide across a brittle solid (Lawn 1967) predict that Auerbach's law should cease to hold when the coefficient of friction between particle and specimen exceeds as little as 0.02: the maximum stress present at fracture does not increase nearly so rapidly as $r^{-\frac{1}{2}}$ as r is decreased. It is therefore probable that microcracking will still be the dominant surface damage and wear mechanism in diamond even with fine abrasives, in agreement with the X-ray evidence.

To Industrial Distributors (Sales) Ltd we are indebted for the provision of specimens and for a Research Grant to one of us (E.M.W.). One author (B.R.L.) wishes to thank British Nylon Spinners and Industrial Distributors (Sales) Ltd. for research fellowships.

REFERENCES

- Dalladay, A. J. 1922 *Trans. Opt. Soc. (Lond.)* **23**, 170.
Evans, T. & Wild, R. K. 1965 *Phil. Mag.* **12**, 479.
Evans, T. & Wild, R. K. 1966 *Phil. Mag.* **13**, 209.
Frank, F. C. & Lawn, B. R. 1967 *Proc. Roy. Soc. A* **299**, 291.
Fukushima, E. 1954 *Acta Cryst.* **7**, 459.
Hamilton, G. M. & Goodman, L. E. 1966 *J. Appl. Mech.* **33**, 371.
Howes, V. R. & Tolansky, S. 1955 *Proc. Roy. Soc. A* **230**, 287, 294.
Kato, N. 1963a In *Crystallography and crystal perfection* (edited by G. N. Ramachandran), pp. 153–173. London: Academic Press.
Kato, N. 1963b *J. Phys. Soc. Jap.* **18**, 1785.
Kato, N. 1964a *J. Phys. Soc. Jap.* **19**, 67.
Kato, N. 1964b *J. Phys. Soc. Jap.* **19**, 971.
Landau, L. D. & Lifshitz, E. M. 1959 *Theory of Elasticity*, pp. 26–29. London: Pergamon.
Lang, A. R. 1959 *Acta Cryst.* **12**, 249.

- Lang, A. R. 1963 *Br. J. Appl. Phys.* **14**, 904.
Lang, A. R. 1964 *Proc. Roy. Soc. A* **278**, 234.
Lang, A. R. 1967 *Nature, Lond.* **213**, 247.
Lawn, B. R. 1967 *Proc. Roy. Soc. A* **299**, 307.
Lawn, B. R., Kamiya, Y. & Lang, A. R. 1965 *Phil. Mag.* **12**, 177.
Lawn, B. R. & Komatsu, H. 1966 *Phil. Mag.* **14**, 689.
Marsh, D. M. 1964 *Proc. Roy. Soc. A* **279**, 420.
Meiran, E. S. & Blech, I. A. 1965 *J. Appl. Phys.* **36**, 3162.
Newkirk, J. B. 1958 *Trans. A.I.M.E.* **215**, 483.
Penning, P. 1966 Thesis, Delft.
Penning, P. & Polder, D. 1961 *Philips Res. Rep.* **16**, 419.
Preston, F. W. 1922 *Trans. Opt. Soc., Lond.* **23**, 141.
Roesler, F. C. 1956 *Proc. Phys. Soc. B* **69**, 55.
Seal, M. 1958 *Proc. Roy. Soc. A* **248**, 379.
Seal, M. 1965 *Industr. Diam. Rev.* **25**, 111.
Takagi, S. 1962 *Acta Cryst.* **15**, 1311.
Tolansky, S. 1966 *Nature, Lond.* **211**, 158.
Tolansky, S. & Austin, E. M. 1949 *Nature, Lond.* **164**, 193.
Tolkowsky, M. 1920 Thesis, University of London.
Twyman, F. 1905 *Proc. Opt. Conv.* p. 52. London: Norgate and Williams.
Wilks, E. M. & Wilks, J. 1959 *Phil. Mag.* **4**, 158.
Wilks, E. M. & Wilks, J. 1965 *Physical properties of diamond* (edited by R. Berman), chap. 8. Oxford: Clarendon.